# Numerical Simulation of Residual Stresses in Multipass Gas Metal Arc-Welded Joints of Thick Aluminum Alloy Plates

*Fengyuan Shu, Lei Wu, Yuxin Liu, Yaohui Lv, Ting Wang, Gang Chen, Fujia Xu, and Binshi Xu*

**Numerical simulation was utilized to investigate the residual stresses in the multipass gas metal arc-welded joints of high-strength Al-Zn-Mg alloy plates. In order to elevate the reliability of numerical simulation, the heat source model, parameters characterizing the thermal and mechanical properties, boundary conditions, material constitutive model and finite element meshing were discussed in detail. As a novelty of this paper, the modified Arrhenius constitutive equation of the base material and the filled material was obtained according to the results of high-temperature tensile tests. Distributions of stress on the upper and bottom surface of the joint were obtained based on numerical simulation. Special attention was paid to the evolutions of local residual stress on the bottom surface of the joint, and it's found that residual stresses on the bottom surface of the joint were almost unchanged after the weld seam approached a certain thickness. Blind-hole method and x-ray method were adopted to detect the residual stresses on the surfaces to verify the accuracy of the results obtained by numerical simulation.**

## 1. Introduction

Al-Zn-Mg aluminum alloys exhibited high specific strength and excellent overall performances after rolling, solution and aging heat treatment (Ref 1, 2). 7A52 aluminum alloy (AA7A52) as this series of aluminum alloy also possessed special and attractive properties including wide quenching temperature range, excellent casting, semi-solid-state and solid-state formability. Therefore, AA7A52 had been widely used in bridges, high-rise buildings, civil engineering structures, military facilities and light amphibious equipment. Welding was used extensively in these industries. However, it was difficult to weld the thick plates of such high-strength aluminum alloy, and the most serious problem was the high residual stresses in the welded joints.

The mechanical properties and service lives of high-strength aluminum alloy-welded structures were greatly affected by residual stress, especially for the structures made by multilayer and multipass welding processes. It was found that shot peening mechanical treatment imparted high induced compressive residual stresses on the surface of the welded joints obtained by shielded metal arc welding (SMAW) and flux cored

arc welding (FCAW) processes, which improved the tensile strength, yield strength and toughness of welded joints (Ref 3). High residual stress was also found to be correlated with the microstructure of the weld seam and heat-affected zone (HAZ) under the condition of low heat input (Ref 4). High tensile residual stress could give birth to worse corrosion resistance of 7075 aluminum alloy laser-welded joints (Ref 5). Meanwhile, residual stress was considered as factor that caused the formation and prolongation of cracks in the welded structure (Ref 6). In literature Ref 7, it's mentioned that the influences of residual stress upon mechanical and chemical properties were dependent upon stress state, and tensile residual stress was often thought harmful to service performances of welded joints. The fatigue lives of weldments under low-load conditions were found obviously shortened because of the existence of tensile residual stresses (Ref 8).

It's difficult to detect the internal stresses in the joint of thick plates, and the inspection cost was high. Recently, numerical simulation had often been used to calculate residual stresses in multipass welded joints of thick plates for its high efficiency and low cost. Moreover, the influences of welding parameters upon residual stress could be quantitatively analyzed based on numerical researches. According to the researches about the narrow-gap welding by finite element method (FEM), heat input obviously affected the peak residual stress while welding speed had significant influences on the width of the tensile stress region (Ref 9). Unlike the stress distributions in two-dimensional model, residual stresses along the three-dimensional and the thickness direction were nonnegligible. Plane strain model, axisymmetric model and lumped-pass three-dimensional (3D) model had been employed to simulate residual stresses in the 300 mm thick narrow-gap weld joint (Ref 10). Results indicated that the peak tensile residual stress along the thickness direction could approach 30% of the peak longitudinal stress. FEM was especially suitable for the investigation of residual stress evolutions in the joints of thick plates. Literature Ref 11 adopted FEM to study the residual

**Fengyuan Shu, Lei Wu, Ting Wang,** and **Gang Chen,** Shandong Provincial Key Laboratory of Special Welding Technology, State Key Laboratory of Advanced Welding and Joining, Harbin Institute of Technology, Weihai 264209, China; **Yuxin Liu, Yaohui Lv,** and **Binshi Xu,** National Key Laboratory of Remanufacturing, Beijing 100072, China; and **Fujia Xu,** Harbin Welding Institute, Harbin 150028, China. Contact e-mail: 3570333103@qq.com.

stresses in the joint of mild steel with a thickness of 6 mm and found that the longitudinal residual stresses along the thickness direction were tensile stress, while the compressive transverse residual stresses appeared in the middle layer of welded joints. Literature Ref 12 studied the residual stresses in thick EH47 plate (50-100 mm) by the FEM and neutron diffraction measurements. Results indicated that the residual stresses along the thickness direction showed an asymmetric parabola distribution, and significant tensile transverse stresses were generated on the upper and bottom surface of the joint. FEM was also adopted to analyze the residual stress distributions in the joint of 20-mm-thick 316L stainless steel, finding that the multipass welding brought a serious work hardening and increased residual stresses (Ref 13).

The constitutive model was used to describe the evolution of stress with strain in the process of material deformation. Researches had obtained the constitutive curves of several aluminum alloy with the assistance of isothermal hot compression and tensile tests. The flow stress of homogenized 7005 aluminum alloy was found to increase when the deformation temperature decreased or elevated strain rate increased according to the isothermal hot compression tests (Ref 14). Through quasi static tension tests, it's found that the 7075-T651 aluminum alloy was more sensitive to temperature than strain rate, and its strength modulus dropped sharply as deformation temperature increased (Ref 15). Inspired by these successful cases, high-temperature tensile tests were adopted to study the constitutive model of 7A52 aluminum alloy and ER5356 welding filler material in this paper.

So as to verify the accuracy of results obtained by numerical simulation, neutron diffraction (ND) measurement, contour method (CM) measurements (Ref 16), x-ray diffraction (XRD) measurement and blind-hole method (Ref 17) were often utilized. The blind-hole and XRD method had been the most popular methods in order to meet the low-cost and high-efficiency requirement. Aiming at obtaining the residual stresses in multilayer and multipass GMA-welded joints of AA7A52 plates, the blind-hole method and XRD method were adopted with combination of FEM in the research.

## 2. Experimental Procedure

### 2.1 Experimental Materials and the Sequence of Welding Passes

The plates with the size of 200 × 150 × 50 mm and welding wire were AA7A52 and ER5356, respectively, whose chemical compositions are listed in Table 1.

The groove was designed as UV-type to reduce the gap, and its specific size is marked in Fig. 1(a). Figure 1(b) presents the sequence of weld passes. The first weld pass, the second to the sixth weld passes, the seventh and eighth weld passes played the role of bottoming, filling and capping welding, respectively. Prior to welding, the surfaces of plates were degreased by wiping with acetone, cleaned with a brush that had stainless bristles, and then dried with a blower. The inter-pass cooling time was set over 150th second, whereas the welding slag was

**Table 1  Chemical composition of selected materials (wt.%)**

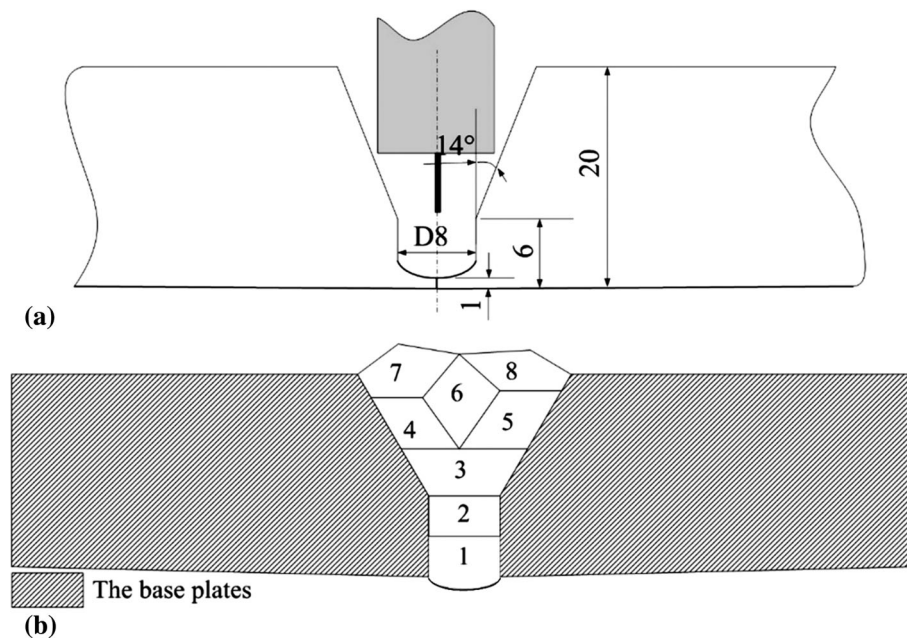|  | Zn | Mg | Cu | Mn | Cr | Ti | Zr | Fe | Si | Al |
|---|---|---|---|---|---|---|---|---|---|---|
| AA7A52 | 4.0-4.8 | 2.0-2.8 | 0.05-0.20 | 0.20-0.50 | 0.15-0.25 | 0.05-0.18 | 0.05-0.15 | ≤ 0.30 | ≤ 0.25 | Balance |
| ER5356 | 0.10 | 4.50-5.50 | 0.10 | 0.05-0.20 | 0.05-0.20 | 0.06-0.20 | … | … | … | Balance |



**Fig. 1**  Schematic diagram of groove design and weld passes, (a) the specific size of the groove (Ref 19), (b) the sequence of weld passes

cleaned up so that the inter-pass temperature was kept below 50 °C and inter-pass contamination was avoided. The welding current and speed of each weld pass are listed in Table 2, and the welding speed was set as 0.2 m/min (Ref 18).

### 2.2 Residual Stress Measurement

The residual stresses on the surface of the joint were measured by blind-hole method and XRD method. YC4 from China was elected as the residual stress measuring device for its high resolution (1 με) and low basic deviation (lower than ± 0.15%). Prior to measuring the surface stress, samples were polished with waterproof abrasive paper to eliminate the oxide film and then electropolished in 10 wt.% NaCl solution to eliminate the effects of the polishing process on the stress distributions.

### 2.3 Tensile Testing

The mechanical properties of material had a great effect on residual stress. In order to obtain the stress–strain curves of material under different temperatures, high-temperature tensile tests using MTS-810 tensile testing machine were carried out according to China National Standard GB/T4338-2006. The size of specimens for high-temperature tensile tests is shown in Fig. 2.

## 3. Establishment of the Model by FEM

### 3.1 Heat Source Model

Cylindrical Gaussian heat source with attenuation coefficient was adopted for the bottoming welding process, while double ellipsoidal heat source was selected for the filling and capping welding process. Equation 1 was the expression of the cylindrical Gaussian heat source with the linear modification coefficient $\xi$, which had been discussed in detail in our previous research Ref 20.

**Table 2   Welding parameters**

| Sequence of weld passes | Function | Welding current, A | Welding speed, m/min |
|---|---|---|---|
| 1 | Bottoming | 240 | 0.2 |
| 2-6 | Filling | 220 | 0.2 |
| 7-8 | Capping | 150 | 0.2 |



**Fig. 2** Schematic size of the high-temperature tensile test specimens

$$q(x,y,z,t) = \frac{3\eta UI}{\pi R^2} \exp\left(\frac{-3x^2}{R^2}\right) \exp\left[\frac{-3(z-vt)^2}{R^2}\right]\left(1 - y\frac{1-\xi}{R}\right)$$

(Eq 1)

### 3.2 Material Parameters of the Base Metal and Filling Metal

The material parameters including thermal conductivity, mass specific heat capacity, surface emissivity and latent heat must be determined precisely in the thermal simulation. The Young's module, thermal expansion, thermal conduct and specific heat capacity of material varying with temperature had been obtained by interpolation calculation and presented in literature Ref 20. To obtain the latent heat of material, it was assumed that the latent heat of materials from solid state to liquid state was equal to that during the reverse transforming process. The equivalent specific heat capacity model mentioned in literature Ref 21 was applied to characterize the latent heat of phase change. In this model, the equivalent specific heat capacity of the material was composed of the inherent specific heat capacity and the increment in specific heat capacity caused by the latent heat of phase change. The latent heat of phase change was evenly distributed in the temperature range of phase change, which could be represented by Eq 2.

$$C_e = \begin{cases} C_s & T < T_s \\ C_s + L_0 & T_L \leq T \leq T_s \\ C_L & T > T_L \end{cases}$$

(Eq 2)

$C_e$, $C_L$, $C_s$, $T_L$, $T_s$ were the equivalent specific heat capacity, the specific heat capacity of liquid phase, the specific heat capacity of solid phase, liquid line and solid line, respectively. $L_0$ was the increment in latent heat caused by the increase in specific heat capacity and could be obtained by Eq 3.

$$L_0 = q(T - T_S)/(T_L - T_S)^2$$

(Eq 3)

The latent heat of alloys could be obtained from the latent heat of each component based on the law of mixing. Therefore, the latent heat of AA7A52 base metal and ER5356 filling wire could be calculated as 447 and 463 kJ/Kg, respectively.

### 3.3 Finite Element Meshing

In order to improve calculation accuracy and save calculation time, refined mesh size was adopted in the welded joint and its vicinity, as shown in Fig. 3. The thermal boundary conditions including heat conduction, heat convection and heat radiation had been comprehensively discussed in literature Ref 22. Angular deformation of welded joints needed to be strictly limited during the welding of thick AA7A52 plates, so the four corners of the plates were rigidly fixed in the simulation to avoid the displacement of the bottom surface along the negative Z axis, which was also detailed in literature Ref 22.

### 3.4 Constitutive Model of the Base Metal and Filled Material

Constitutive model described the evolution of stress with strain during deformation. The plastic deformation behavior of aluminum alloys at high temperature could be described by the modified Arrhenius constitutive equation, which expressed the
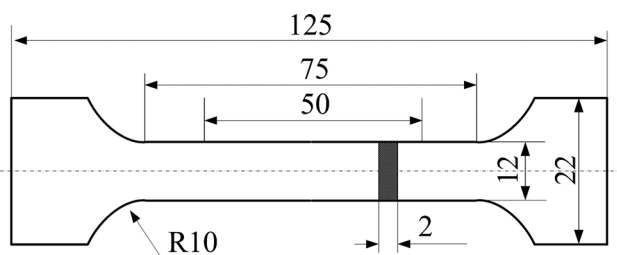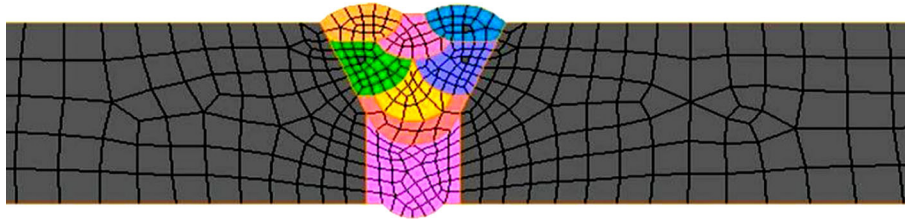
**Fig. 3** Elements of the FEM model for multipass GMA welding

relationship between strain rate $\varepsilon'$, temperature $T$ and flow stress $\sigma$ (Ref 23). The expression was presented as Eq 4 where the effects of deformation activation energy and temperature on the deformation behavior of the material were taken into account from the perspective of rheological dynamics.

$$\varepsilon' = AF(\sigma)\exp\left(-\frac{Q}{RT}\right) \tag{Eq 4}$$

$F(\sigma)$, $A$, $R$, $T$ and $Q$ were the function of stress, temperature-independent constant, Clapeyron gas constant, absolute temperature and deformation activation energy, respectively. The relationships between stress and strain rate could be illustrated by exponential equation at low-stress level and power-exponent equation at high-stress level, as shown in Eq 5 and 6, respectively. Both the equations could be converted to Eq 7 within the entire stress range (Ref 24).

$$F(\sigma) = A_1\sigma^{n_1} \tag{Eq 5}$$

$$F(\sigma) = A_2\exp(\beta\sigma) \tag{Eq 6}$$

$$F(\sigma) = A_3[\sinh(\alpha\sigma)]^{n_2} \tag{Eq 7}$$

Among these three equations, $A_1$, $A_2$, $A_3$, $n_2$, $n_1$, $\alpha$ and $\beta = n_1\alpha$ were all temperature-independent constants. Equation 8, 9 and 10 could be obtained when Eq 5, 6 and 7 were substituted into Eq 4, respectively.

$$\varepsilon' = A_1\sigma^{n_1}\exp\left(-\frac{Q}{RT}\right) \tag{Eq 8}$$

$$\varepsilon' = A_2\exp(\beta\sigma)\exp\left(-\frac{Q}{RT}\right) \tag{Eq 9}$$

$$\varepsilon' = A_3[\sinh(\alpha\sigma)]^{n_2}\exp\left(-\frac{Q}{RT}\right) \tag{Eq 10}$$

The value of $\alpha\sigma$ was used to indicate the level of stress during plastic deformation process. With regard to the high-temperature rheological behaviors of Al-Zn-Mg aluminum alloys, $\alpha\sigma \leq 0.8$ and $\alpha\sigma \geq 1.2$ could be identified as low-stress and high-stress level, respectively (Ref 25).

Besides, Zener–Hollomon parameter was adopted to characterize the effects of the deformation temperature and deformation rate on the deformation. Z represented the temperature-compensated strain rate; that is, the deformation process could be controlled by different combinations of temperature and strain rate. Its expression is shown in Eq 11.

$$Z = \varepsilon'\exp\left(\frac{Q}{RT}\right) = A_3[\sinh(\alpha\sigma)]^{n_2} \tag{Eq 11}$$

### 3.5 Determination of Parameters in Constitutive Model

Equation 12, 13, 14 and 15 could be obtained when logarithmic operation was applied to Eq 8, 9, 10 and 11, respectively.

$$\ln\varepsilon' = \ln A_1 + n_1\ln\sigma - \frac{Q}{RT} \quad \text{(low - stress level)} \tag{Eq 12}$$

$$\ln\varepsilon' = \ln A_2 + \beta\sigma - \frac{Q}{RT} \quad \text{(high - stress level)} \tag{Eq 13}$$

$$\ln\varepsilon' + \frac{Q}{RT} = \ln A_3 + n_2\ln[\sinh(\alpha\sigma)] \tag{Eq 14}$$

$$\ln A_3 = \ln\varepsilon' + \frac{Q}{RT} - n_2\ln[\sinh(\alpha\sigma)] \tag{Eq 15}$$

Then $n_1 = \frac{\partial\ln\varepsilon'}{\partial\ln\sigma}$ and $\beta = \frac{\partial\ln\varepsilon'}{\partial\sigma}$ could be calculated. $n_2$ could be represented by Eq 16 when the temperature in Eq 14 was set as constant, whereas $Q/Rn_2$ could be described as Eq 17 when the strain rate was constant. Equation 18 could be obtained by substituting Eq 13 into Eq 14.

$$n_2 = \left[\frac{\partial\ln\varepsilon'}{\partial\ln\sinh(\alpha\sigma_T)}\right]_T \tag{Eq 16}$$

$$\frac{Q}{Rn_2} = \left[\frac{\partial\ln\sinh(\alpha\sigma)}{\partial(1/T)}\right]_\varepsilon \tag{Eq 17}$$

$$Q = R\left[\frac{\partial\ln\varepsilon'}{\partial\ln\sinh(\alpha\sigma_T)}\right]_T\left[\frac{\partial\ln\sinh(\alpha\sigma)}{\partial(1/T)}\right]_\varepsilon \tag{Eq 18}$$

When the temperature was constant, $n_1$ was the slope of the $\ln\varepsilon' - \ln\sigma$ curve and $\beta$ that of the $\ln\varepsilon' - \sigma$ curve. Therefore, $n_1$ and $\beta$ could be obtained by linearly fitting the curves between $\ln\varepsilon'$ and $\ln\sigma$, $\ln\varepsilon'$ and $\sigma$, $1/T$ and $\ln(\sinh(\alpha\sigma))$, $\ln\varepsilon'$ and $\ln[\sinh(\alpha\sigma)]$ according to the experimental data.

Figure 4 exhibits the true stress–strain curves of 7A52 aluminum alloy during hot tensile deformation under different temperatures and strain rates. As shown in Fig. 4, the curves directly turned into the plastic deformation stage from the elastic deformation stage without obvious yield process. Besides, work hardening and dynamic softening owing to dislocation pile-ups and dynamic recrystallization of dislocations were observed.

Therefore, the stress–strain curve of the material was actually the comprehensive effect of work hardening and dynamic softening. The hardening characteristic of the material was weakened and gradually replaced by dynamic softening as
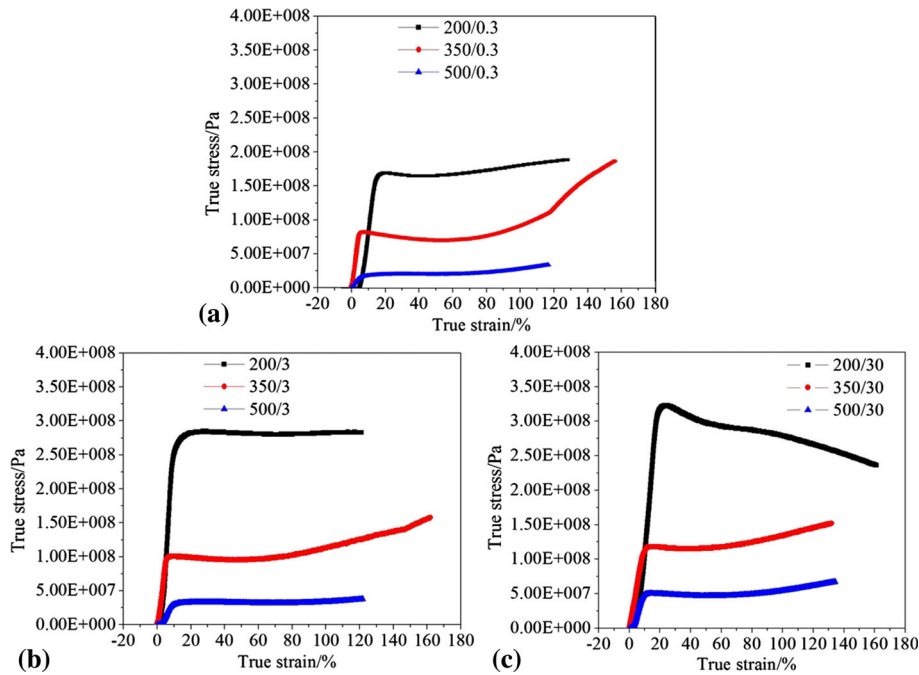
**Fig. 4** True stress–strain curves of AA7A52 under different temperatures (°C) and strain rates, (a) under constant strain rate of 0.3 m/min, (b) under constant strain rate of 3 m/min, (c) under constant strain rate of 30 m/min

temperature increased. As a result, the curve entered the steady-state rheological stage more quickly, which was consistent with the results of 7050 aluminum alloy (Ref 26). When the strain rate was constant, the peak flow stress decreased as deformation temperature increased. When the deformation temperature was constant, the peak flow stress increased as the strain rate increased. When $\varepsilon$ exceeded 20%, the curve turned into a stable stage where the flow stresses changed little under different temperatures. The relation charts about $\ln \varepsilon'$ and $\sigma$, $\ln \varepsilon'$ and $\ln\sigma$, $\ln \varepsilon'$ and $\ln [\sinh (\alpha\sigma)]$, as shown in Fig. 5(a), (b) and (c), could be obtained by submitting $\varepsilon = 20\%$ into Eq 12, 13 and 14, respectively. By averaging the growth rates of $\ln \varepsilon'$ and $\sigma$, $\ln \varepsilon'$ and $\ln\sigma$, $\ln \varepsilon'$ and $\ln [\sinh (\alpha\sigma)]$ under different temperatures, $n_1 = 7.9$, $\beta = 0.107$, $n_2 = 6.13$, $\alpha = \beta/n_1 = 0.0135$ were obtained. Figure 5(d) presents the linear relationship between $\ln(\sinh(\alpha\sigma))$ and $1/T$ which proved the Arrhenius relationship between stress and temperature.

Equation 19 could be obtained by taking the logarithm of Eq 11. By substituting $\alpha$ and the stress value into Eq 11 when $\varepsilon = 20\%$, the value of $Z$ under different temperatures and strain rates could be obtained, after which the relationship curve between $\ln Z$ and $\ln [\sinh (\alpha\sigma)]$ could be plotted. As can been seen from Eq 19, $\ln A$ and $n_2$ were the intercept and slope of the curve, respectively, so the structural factor $A = 2.32 \times 10^{11}$ could be obtained. Then substituting $Q$, $n$, $A$ and $\alpha$ into Eq 13, the constitutive equation of the alloy could be obtained and expressed as Eq 20.

$$\ln Z = \ln A + n_2 \times \ln [\sinh(\alpha\sigma)] \qquad (\text{Eq 19})$$

$$\begin{aligned}\varepsilon' &= A [\sinh (\alpha\sigma)]^{n_2} \exp\left(-\frac{Q}{RT}\right) \\ &= 2.32 \times 10^{11} \times \sinh^{6.13}(0.0135 \times \sigma) \times \exp\frac{-46.8}{T}\end{aligned}$$
$$(\text{Eq 20})$$

Similarly, $Q$, $n_2$, $A$ and $\alpha$ of filled material were calculated as 210 kJ/mol, 6.5, $6.8 \times 10^{13}$ and 0.019, respectively, so the constitutive equation of the filled material could be expressed as Eq 21.

$$\begin{aligned}\varepsilon' &= A [\sinh (\alpha\sigma)]^{n_2} \exp\left(-\frac{Q}{RT}\right) \\ &= 6.8 \times 10^{13} \times \sinh^{6.5}(0.019 \times \sigma) \times \exp\frac{-25.3}{T}\end{aligned} \qquad (\text{Eq 21})$$

## 4. Results and Discussions

### 4.1 Evolution Process of Residual Stress Field

The direction of longitudinal stress was parallel to the weld seam, while that of transversal stress was perpendicular to the weld seam. The evolution of three-dimensional stress field in the joint could be characterized by the two-dimensional stress distributions on the upper surface, the bottom surface and the middle cross section. Figure 6 presents the distributions of transverse and longitudinal stress on the upper surface of welded joint at different time. The middle and ends of the weld seam were subjected to transverse tensile stresses and small transverse compressive stresses during the entire cooling process, respectively. A dumbbell-shaped longitudinal tensile stress zone formed around the weld seam and narrowed gradually with the increase in weld passes.

Figure 7 presents the distributions of transverse stress on the bottom surface of the joint at different time. The bottom surface of the joint was subjected to tensile transverse stresses when the first weld pass was completed. The peak tensile transverse stress dropped obviously when the second weld pass was completed and remained unchanged generally in the subsequent welding.
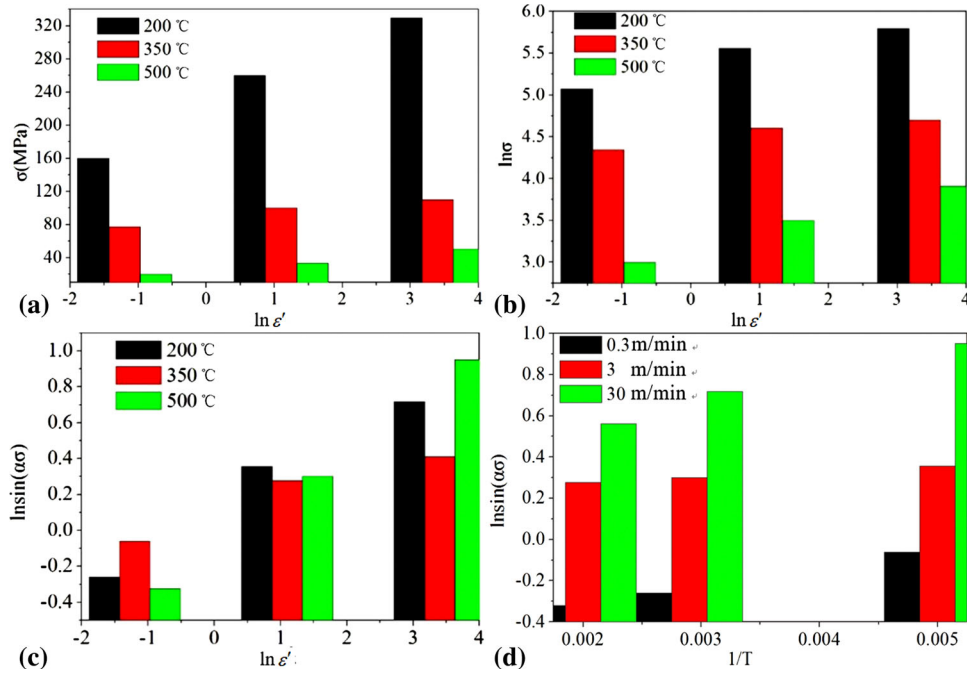
**Fig. 5** Relationships between obtained parameters under different temperatures, (a) $\sigma$ and $\ln\dot{\varepsilon}$, (b) $\ln\sigma$ and $\ln\dot{\varepsilon}$, (c) $\ln\dot{\varepsilon}$ and $\ln[\sinh(\alpha\sigma)]$ and temperatures, (d) $\ln(\sinh(\alpha\sigma))$ and $1/T$
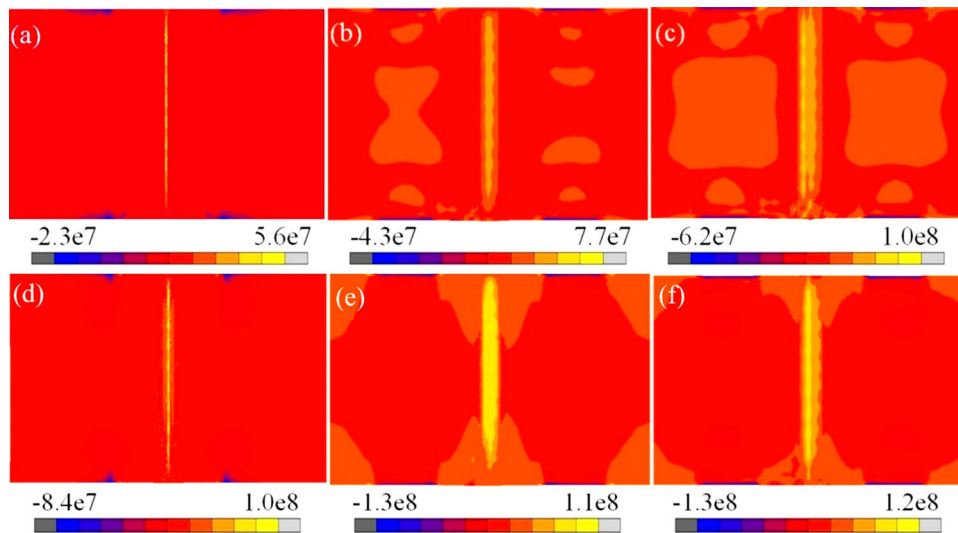


**Fig. 6** Distributions of transverse stress and longitudinal stress on the upper surface of welded joint at different time steps, (a) transverse stress, $t = 50$ s, (b) transverse stress, $t = 300$ s, (c) transverse stress, $t = 500$ s, (d) longitudinal stress, $t = 50$ s, (e) longitudinal stress, $t = 300$ s, (f) longitudinal stress, $t = 500$ s

Figure 8 presents the distributions of longitudinal stress on the bottom surface of the joint at different time. The bottom surface of the joint was always subjected to tensile longitudinal stresses and the area of longitudinal stress shrunk as the weld passes increased. The peak longitudinal stress decreased gradually and closed to 0 when all weld passes were finished.

### 4.2 Distribution of Residual Stress

In Cartesian coordinates, the direction of longitudinal stress and transverse stress was along the positive Z axis and X axis, respectively, as shown in Fig. 9. The residual stress distribu-

tions along the thickness direction, the transverse direction and the longitudinal direction were represented by the residual stress distributions along TD, CO and F1B1 (F1B2) paths, respectively.

The distributions of longitudinal residual stress along DT, CO, F1B1 and F2B2 paths are shown in Fig. 10. Because the free shrinkage during cooling was limited, the bottom surface of the joint was subject to tensile stresses initially. As the completed weld passes increased, their restriction on the deformation of the upper weld seam enhanced, resulting in the generation of compressive stresses on the bottom surface of the joint and tensile stresses on the upper surface of the joint.
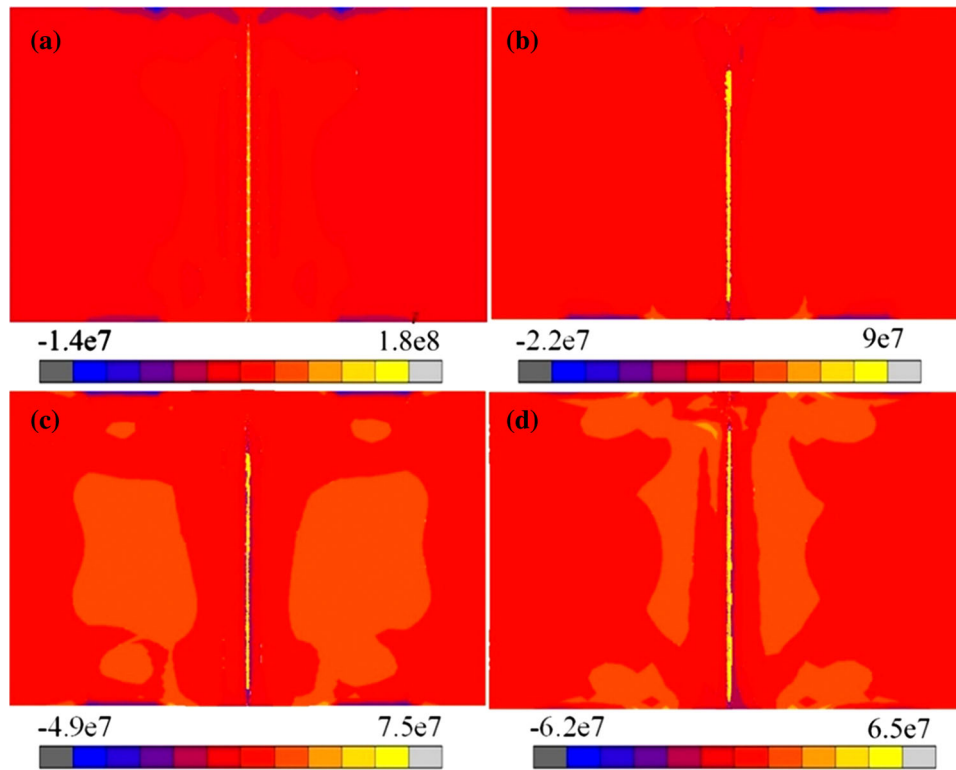
**Fig. 7** Distributions of transverse stress on the bottom surface of welded joints at different times, (a) $t = 50$ s, (b) $t = 150$ s, (c) $t = 320$ s, (d) $t = 1250$ s
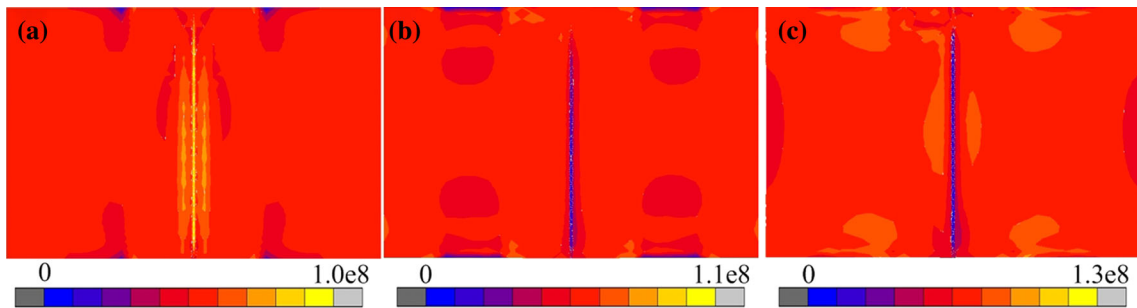


**Fig. 8** Distributions of longitudinal stress on the bottom surface of welded joints, (a) $t = 50$ s, (b) $t = 100$ s, (c) $t = 500$ s
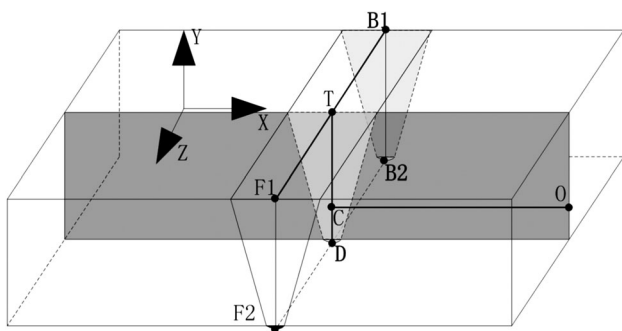


**Fig. 9** Diagram of stress distribution path in finite element model

The residual stresses in thick plates were determined by both the evolution of stress field and the balance requirement of internal moments and stresses, the latter caused the tensile longitudinal stresses on the bottom surface of the joint to gradually decreased and drop to 50 MPa finally.

The longitudinal stresses along path CO rose rapidly and then decreased as shown in Fig. 10(b). The longitudinal stresses along path F1B1 and path F2B2 exhibited a stable zone with slight fluctuation as shown in Fig. 10(c) and (d). The longitudinal tensile stress along path F1B1 was large in the middle and small on both sides, while that along path F2B2 was reversed. The longitudinal residual stresses fluctuated with large amplitude along the thickness direction (path DT) while low tensile stresses close to zero were observed on the bottom surface of the joint as shown in Fig. 10(a).

The distribution of transverse residual stress along path F1B1 is depicted in Fig. 11, and the middle of the path was subjected to tensile stresses, while ends were subjected to compressive stresses.
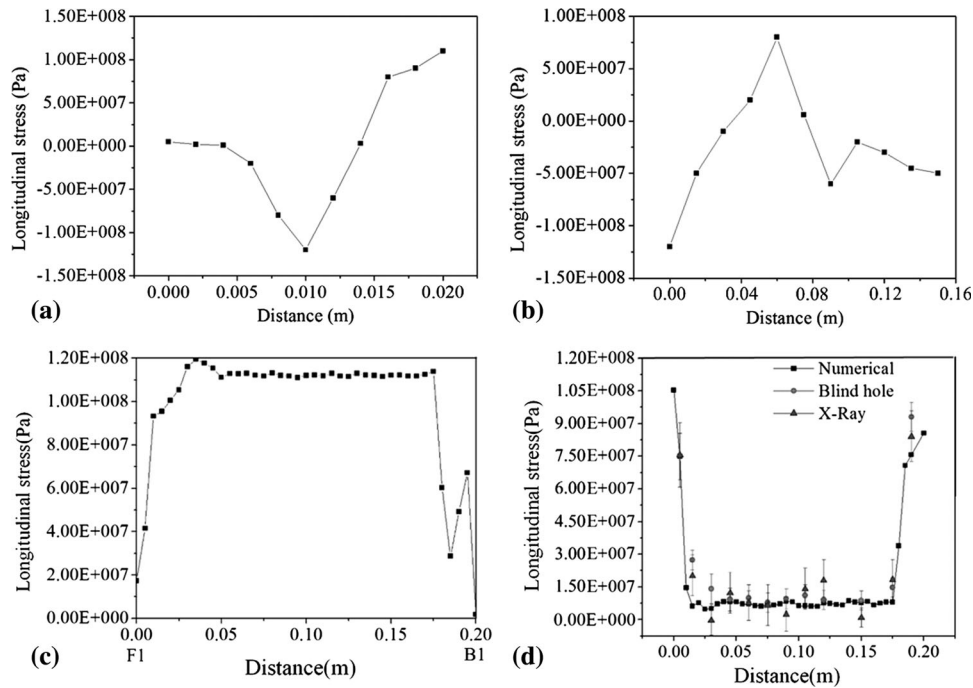
**Fig. 10** Distributions of longitudinal residual stress along specific paths, (a) DT, (b) CO, (c) F1B1, (d) F2B2
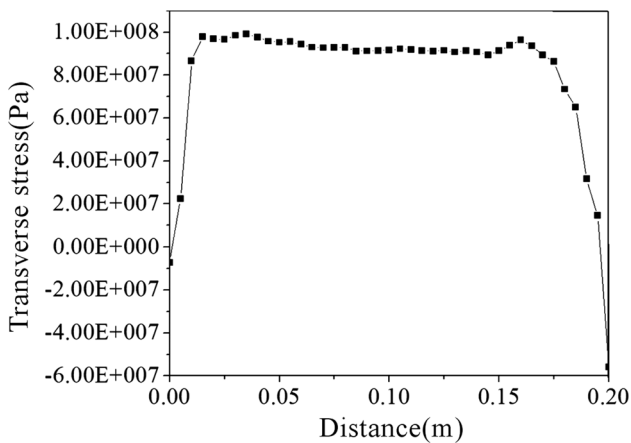


**Fig. 11** Distribution of transverse residual stress along the path F1B1

### 4.3 None Transformation of Stress State on the Bottom Surface of the Joint

For the multilayer and multipass GMA welding of thick plates, the completed weld passes played a decisive role in the distributions of residual stress. It was mentioned in some literatures that the residual stress distributions on the bottom surface of the joint reached the steady state close to the final distributions when the thickness of the finished weld seam reached 1/3 of the thickness of the plate (Ref 27, 28). In our research, the tensile transverse stress on the bottom surface of welded joints was reduced by 50 MPa and 30 MPa when the second weld pass and the third weld pass were completed, respectively, as shown in Fig. 13(a). The thickness of the weld seam reached 13 mm when the third weld pass got completed, and the transverse residual stress on the bottom surface of the joint reached the stable stage (70 MPa) with small fluctuation
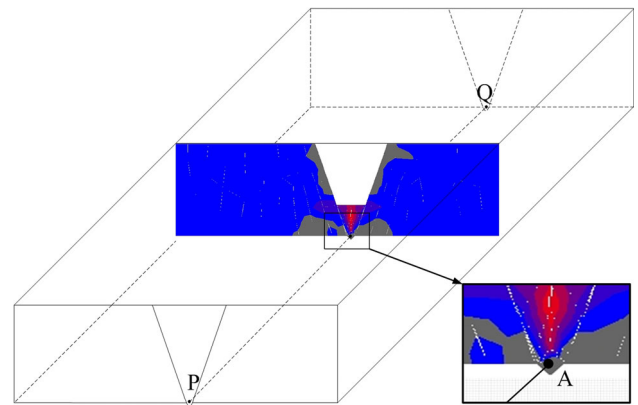


**Fig. 12** Schematic of the location of point A

(less than 5 MPa) as shown in Fig. 13(a). It could be observed from Fig. 13(a) that there was none transformation from tensile stress to compressive stress on the bottom surface of the weld seam, which could be attributed to two reasons. Firstly, the UV-type groove reduced the volume difference between filled material of each layer, lessening the sub-layer inhomogeneity of plastic deformation in the weld seam along the longitudinal direction. Secondly, the heat source was quickly moved away because of the high filling metal efficiency of GMA welding, so the subsequent weld bead had weaker heat treatment effect on the bottom surface of the joint, which led to weakened stress release in the first weld pass.

### 4.4 Local Stress Evolution in the Bottom Surface of Welded Joints

Point A located in the middle cross section was chosen to study the local stress evolutions on the bottom surface of the joint as shown in Fig. 12. Figure 13(a) presents the evolution

of plastic strain and residual stress at point A. The transverse stress exhibited small compressive stress (about 0.43 MPa) during the heating process of the first weld pass. Ignoring the formation of the weld pool, the weld seam was subjected to transverse tensile stress and its plastic transverse tensile strain increased rapidly during cooling. Besides, the plastic tensile strain remained unchanged after the 270th second during which period the temperature was below 170 °C as seen in Fig. 13(b). That's because the material strength was regained with the temperature dropping and the tensile residual stress was thus too low to overwhelm the yield strength of the material and prolong the plastic deformation process.

The generation of residual plastic deformation was related to temperature, and there was a temperature interval in which residual plastic deformation occurred. When the temperature exceeded the melting point, the weld seam was identified completely plastic. Therefore, the melting point could be used as the upper critical temperature above which the residual plastic deformation could not be retained. The bottom critical temperature $T_e$ could be determined by Eq 22, 23 and (24). Firstly, the internal strain of the area could be expressed as Eq 22.

$$\varepsilon = \varepsilon_e - \varepsilon_T \qquad (Eq\ 22)$$

$\varepsilon$, $\varepsilon_e$ and $\varepsilon_T$ were the internal strain, appearance strain and free strain, respectively, and $\varepsilon_e$ was taken to 0 under rigid constraints. When the temperature reached $T_e$, the $\varepsilon$ of area A reached the maximum elastic strain $\varepsilon_s$. Before the temperature reached $T_e$, the $\varepsilon_T$ of area A was in the elastic phase during which period the strain was linearly related to the change of temperature, as shown in Eq 23.

$$\varepsilon_T = \alpha(T - T_0) \qquad (Eq\ 23)$$

$\alpha$ and $T_0 = 0$ °C were the thermal expansion coefficient at room temperature and the initial temperature, respectively.

Only considering the value of strain, Eq 24 could be obtained through substituting $T_e$ into Eq 22 and 23.

$$T_e = \frac{\sigma_s}{E\alpha} \qquad (Eq\ 24)$$

$\sigma_s$, $E$ and $\alpha$ were the yield strength, elastic modulus and thermal expansion coefficient of the material at room temperature, respectively.

When the heating temperature was lower than $T_e$, the residual stress substantially remained unchanged because no plastic strain generated. Figure 13(b) presents the thermal cycle curve at point A, the maximum heating temperature since the 270th second was 170 °C which was below than 240 °C the calculated value of $T_e$. The point A was in the elastic deformation stage, so the transverse residual stress was related to the modulus changing with temperature since the 270th second. In addition, the transverse residual stress at point A was also affected by structural balance, although stress was not high enough to produce obvious plastic strain at low temperature, low tensile stress or even the compressive stress would generate to keep the structural balance.

It could be seen from Fig. 4 that the work hardening of the material occurred under the large strain condition. The welding heat source provided a large amount of energy for dislocation slip, so the work hardening due to plastic deformation during welding was small. Meanwhile, dynamic softening played a more significant role as temperature increased. The temperature was so high during welding that the yield strength of the material was close to 0, which could be regarded as the completely plastic material. Therefore, dynamic softening played a dominant role during welding, which inevitably contributed to the generation of plastic strain during the cooling process, thereby facilitating the release of residual stresses and reducing the residual stresses in the weld seam. When the first weld pass was completed, the maximum transverse tensile stress reached 180 MPa lower than the yield strength. Then the first weld seam got heat-treated during the second weld pass, the yield strength of the material decreased with temperature rising according to the material constitutive model, and stress relaxation occurred when the yield strength was lower than transverse tensile stresses. After that, the shrinkage of the weld seam was restricted during cooling, thus the first weld seam was subjected to transverse tensile stresses again. Besides, the reduction of transverse tensile stresses in the first weld seam was related to compression from subsequent weld passes during cooling. Obviously, the compression from the following weld seam was enhanced with the increase in weld passes. As a conclusion of the above discussions, the decrement in transverse tensile stresses in the first weld seam could be attributed to the stress relaxation during the heating stage of subsequent welding process and compression from subsequent weld passes during cooling. In addition, the decrement in transverse tensile stresses in the first weld seam caused by the subsequent weld passes became decelerated after the fourth weld pass was completed, whereas the influence of the seventh and eighth weld passes upon the peak transverse tensile transverse stresses
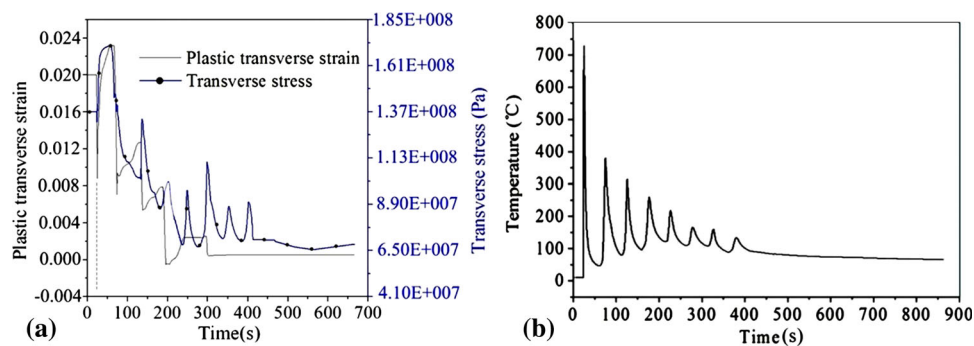


**Fig. 13** Evolution of response variables as cooling down, (a) plastic transverse strain and transverse stress at point A, (b) temperature evolution curve at point A
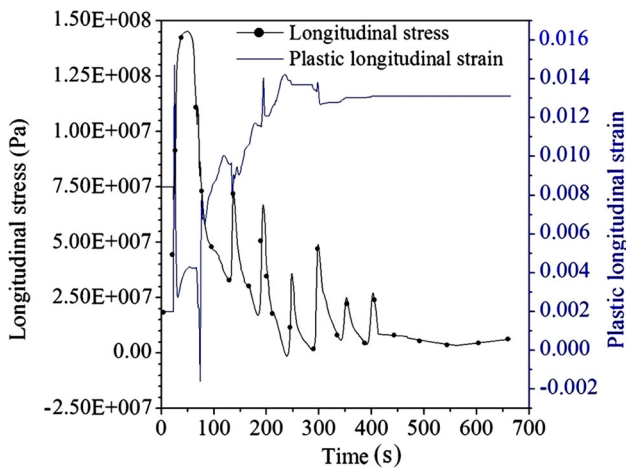
**Fig. 14** Evolution curve of plastic longitudinal strain and longitudinal stress at point A

was the weakest. It should be explained by the following two aspects: firstly, the heat treatment effect on the first weld seam was weakened as welding passes increased, which reduced the extent of stress relaxation. Secondly, the fourth weld pass didn't achieve the connection of the base plates as shown in Fig. 1(b), so the restriction on the shrinkage of the fourth weld pass from the base plates was weaker as compared with the second and the third weld passes.

The evolution of longitudinal stress and longitudinal plastic strain at point A is shown in Fig. 14. The first weld seam was subjected to longitudinal tensile stress during the entire welding process. The yield strength decreased along as temperature rising during the second heating stage. As a result, plastic deformation generated and led to the release of longitudinal stress. Besides, the longitudinal plastic strain reached a stable value when the fifth weld pass was completed at the 360th second, which was similar to the evolution of longitudinal transverse plastic strain. The longitudinal tensile stress decreased firstly and then increased during every subsequent thermal cycling after the 360th second. Macroscopically, the tensile longitudinal stress decreased slowly with the increase in weld passes.

## 5. Comparison with Experimental Measurements

Blind-hole method and XRD method were often used to verify the accuracy of the numerical simulation (Ref 10, 29, 30). Though calculations and measurements, the numerical results were in well agreement with that obtained by blind-hole method and XRD method as indicated in Fig. 10(d). The average longitudinal residual stress in the steady stage obtained by numerical simulation was 7.5Mpa, while that obtained by blind-hole method and XRD method were around 10 MPa and 12 MPa, respectively. Besides, the longitudinal residual stresses in the steady stage obtained by XRD method fluctuated violently with the maximum and minimum stress detected as 25.5Mpa and − 7.5Mpa, respectively. Therefore, the XRD method was often adopted for qualitative analysis because of the large deviations, while the blind-hole method for quantitative analysis to detect actual residual stress distributions.

The residual stresses were mainly caused by inhomogeneous plastic deformation during welding. While the external mechanical constraint was defined as rigid fixation in simulation, ideal rigid fixation was rarely achieved during the actual welding process, which caused small macroscopic deformation of the joint and stress relaxation of the weld seam. In addition, although the blind holes were obtained though strict experimental process, the results were inevitably affected by the sensitivity of the strain gauge and the flatness of the tested surface. Therefore, difference was also inevitable between the results obtained by blind-hole method and that predicted by FEM.

## 6. Conclusion

(1) The modified Arrhenius equations were obtained according to the constitutive model of the base material and the filled material. Work hardening and dynamic softening occurred simultaneously during plastic deformation, whereas the latter gradually played the dominant role as the deformation temperature increased. The flow stresses increased rapidly, approached the peak value, and finally dropped down to the steady stage during the plastic deformation process. The deformation temperature and strain rate were found to have contrary effects upon the peak flow stresses.

(2) The middle and end regions on the upper surface of the weld seam were subjected to transverse tensile stresses and small transverse compressive stresses during the entire welding process, respectively. A dumbbell-shaped longitudinal tensile stress zone formed around the weld seam and narrowed gradually with the increase in weld passes.

(3) The bottom surface of the weld joint was always subjected to tensile stresses during the entire welding process and the area of longitudinal stress shrunk as the weld passes increased. The peak transverse tensile stress dropped obviously when the second weld pass was completed and remained unchanged generally in the subsequent welding. The peak longitudinal stress decreased gradually and closed to 0 when all welding passes were finished.

(4) There was none transformation from tensile stress to compressive stress on the bottom surface of the joint, which could be attributed to two reasons: Firstly, the UV-type groove lessened the sub-layer inhomogeneity of plastic deformation in the weld seam along the longitudinal direction. Secondly, the heat treatment effect on the bottom surface of the joint caused by the subsequent weld passes was weaker and weaker as the heat source rose quickly.

# References

1. Y. Feng, J. Chen, W. Qiang, and K. Wang, Microstructure and Mechanical Properties of Aluminium Alloy 7A52 Thick Plates Welded by Robotic Double-Sided Coaxial GTAW Process, *Mater. Sci. Eng. A*, 2016, **73**, p 8–15

2. S. Zhou, L. Wang, L.Y. Xie, and X.U. Liang, Effect of T7951 Secondary Aging Treatment on Crack Propagation Behavior of 7055 Aluminum Alloy, *Trans. Nonferrous Met. Soc. China*, 2016, **26**(4), p 938–944

3. A.D.S. Lins, L.F.G.D. Souza, and M.C. Fonseca, Characterization of Mechanical Properties and Residual Stress in API, 5L X80 Steel Welded Joints, *J. Mater. Eng. Perform.*, 2018, **27**(1), p 124–137

4. H. Alipooramirabad, R. Ghomashchi, A. Paradowska, and M. Reid, Residual Stress- Microstructure- Mechanical Property Interrelationships in Multipass HSLA Steel Welds, *J. Mater. Process. Technol.*, 2016, **231**, p 456–467

5. K. Liu, J.T. Wang, Y.K. Zhang, J.F. Chen, J.Y. Zhou, M.Z. Ge, Y.L. Lu, and X.L. Li, Effects of Laser Shock Peening On Stress Corrosion Behavior of 7075 Aluminum Alloy Laser Welded Joints, *Mater. Sci. Eng. A*, 2015, **647**, p 7–14

6. H.W. Ahmad, J.H. Hwang, J.H. Lee, and D.H. Bae, Welding Residual Stress Analysis and Fatigue Strength Assessment of Multi-pass Dissimilar Material Welded Joint Between Alloy 617 and 12Cr Steel, *Metals*, 2018, **8**(1), p 21

7. P. Ferro and F. Berto, Quantification of the Influence of Residual Stresses on Fatigue Strength of Al-Alloy Welded Joints by Means of the Local Strain Energy Density Approach, *Strength Mater.*, 2016, **48**(3), p 426–436

8. D. Ngoula, H.T. Tchoffo, and M.Vormwald Beier, Fatigue Crack Growth in Cruciform Welded Joints: Influence of Residual Stresses and of the Weld Toe Geometry, *Int. J. Fatigue*, 2017, **101**, p 253–262

9. A.S. Elmesalamy, H. Abdolvand, J.N. Walsh, J.A. Francis, W. Suder, S. Wolliams, and L. Li, Measurement and Modelling of the Residual Stresses in Autogenous and Narrow Gap Laser Welded AISI, Grade 316L Stainless Steel Plates, *Int. J. Press Vessels Piping*, 2016, **147**, p 64–78

10. C. Liu, J. Yang, Y. Shi, Q. Fu, and Y. Zhao, Modelling of Residual Stresses in a Narrow-Gap Welding of Ultra-Thick Curved Steel Mockup, *J. Mater. Process. Technol.*, 2018, **256**, p 239–246

11. K. Ikushima and M. Shibahara, Prediction of Residual Stresses in Multi-pass Welded Joint Using Idealized Explicit FEM Accelerated by a GPU, *Comput. Mater. Sci.*, 2017, **93**(93), p 62–67

12. W.C. Jiang, W.C. Woo, Y. Wan, Y. Luo, X.F. Xie, and S.T. Tu, Evaluation of Through-Thickness Residual Stresses by Neutron Diffraction and Finite-Element Method in Thick Weld Plates, *ASME J. Press. Vessel Technol.*, 2017, **139**(3), p 031401

13. W.C. Jiang, Y. Luo, B.Y. Wang, W.C. Woo, and S.T. Tu, Neutron Diffraction Measurement and Numerical Simulation to Study the Effect of Repair Depth on Residual Stress in 316L Stainless Steel Repair Weld, *ASME J. Press. Vessel Technol.*, 2015, **137**(4), p 041406

14. L. Chen, G. Zhao, J. Yu, and W. Zhang, Constitutive Analysis of Homogenized 7005 Aluminum Alloy at Evaluated Temperature for Extrusion Process, *Mater. Des.*, 2015, **66**, p 129–136

15. K. Senthil, M.A. Iqbal, P.S. Chandel, and N.K. Gupta, Study of the Constitutive Behavior of 7075-t651 Aluminum Alloy, *Int. J. Impact Eng.*, 2017, **108**, p 171–190

16. Y. Wan, W.C. Jiang, J. Li, G.G. Sun, D.K. Kim, W.C. Woo, and S.T. Tu, Weld Residual Stresses in a Thick Plate Considering Back Chipping: Neutron Diffraction, Contour Method and Finite Element Simulation Study, *Mater. Sci. Eng. A*, 2017, **699**, p 62–70

17. C.O.D. Martins, T.R. Strohaecker, A.S. Rocha, and T.K. Hirsch, Application of x-ray Diffraction, Micromagnetic and Hole Drilling Methods for Residual Stress Determination in a Ball Bearing Steel Ring, *Exp. Mech.*, 2005, **45**(4), p 344–350

18. F.Y. Shu, Y.M. Sun, H.Y. Zhao, X.G. Song, S.H. Sui, and W.X. He, Microstructural and Mechanical inhomogeneity in the narrow-gap weld seam of thick GMA welded Al-Zn-Mg Alloy Plates, *J. Mater. Res.*, 2016, **31**(24), p 3948–3955

19. F.Y. Shu, Y.H. Lv, Y.X. Liu, F.J. Xu, Z. Sun, P. He, and B.S. Xu, Residual Stress Modeling of Narrow Gap Welded Joint of Aluminum Alloy by Cold Metal Transferring Procedure, *Constr. Build. Mater.*, 2014, **54**(54), p 224–235

20. H. Liu, S.Q. Zhang, F.Y. Shu, Y.M. Sun, Q.T. Guo, H.Y. Zhao (2017) Groove Design and Modified Heat Source Model for Welding Thick Architectural Structure Plates by Narrow-Gap Mig Method. In 70th IIW International Conference on Green Welding Technologies for Effective and Reliable Manufacturing, p 552–557. Shanghai

21. T. Kousksoua, A. Jamil, and Y. Zeraouli, Enthalpy and Apparent Specific Heat Capacity of the Binary Solution During the Melting Process: DSC Modeling, *Thermochim. Acta*, 2012, **541**(15), p 31–41

22. F.Y. Shu, Y.H. Lv, Y.X. Liu, F.J. Xu, Z. Sun, P. He, and B.S. Xu, FEM Modeling of Softened Base Metal in Narrow-Gap Joint by CMT+P MIX Welding Procedure, *Trans. Nonferrous Met. Soc. China*, 2014, **24**(6), p 1830–1835

23. C.Q. Huang, J. Deng, S.X. Wang, and L.L. Liu, A Physical-Based Constitutive Model to Describe the Strain-Hardening and Dynamic Recovery Behaviors of 5754 Aluminum Alloy, *J. Mater. Sci. Eng. A*, 2017, **699**, p 106–113

24. L. Saravanan and T. Senthilvelan, Constitutive Equation and Microstructure Evaluation of an Extruded Aluminum Alloy, *J. Mater. Res. Technol.*, 2016, **5**(1), p 21–28

25. H.R.R. Ashtiani and P. Shahsavari, Strain-Dependent Constitutive Equations to Predict High Temperature Flow Behavior of AA2030 Aluminum Alloy, *Mech. Mater.*, 2016, **100**, p 209–218

26. B. Wu, M.Q. Li, and D.W. Ma, The Flow Behavior and Constitutive Equations in Isothermal Compression of 7050 Aluminum Alloy, *Mater. Sci. Eng. A*, 2012, **542**(18), p 79–87

27. J. Zhang, P. Dong, F.W. Brust, W.J. Shack, M.E. Mayfield, and M. Mcneil, Modeling of Weld Residual Stresses in Core Shroud Structures, *Nucl. Eng. Des.*, 1997, **195**(2), p 171–187

28. S. Paddea, J.A. Francis, A.M. Paradowska, P.J. Bouchard, and I.A. Shibli, Residual Stress Distributions in a P91 Steel-Pipe Girth Weld Before and After Post Weld Heat Treatment, *Mater. Sci. Eng. A*, 2012, **534**(1), p 663–672

29. Q. Wang, X.S. Liu, P. Wang, X. Xiong, and H.Y. Fang, Numerical Simulation of Residual Stress in 10Ni5CrMoV Steel Weldments, *J. Mater. Process. Technol.*, 2017, **240**, p 77–86

30. S.Y. Hwang, Y. Kim, and J.H. Lee, Finite Element Analysis of Residual Stress Distribution in a Thick Plate Joined Using Two-Pole Tandem Electro-Gas Welding, *J. Mater. Process. Technol.*, 2016, **229**, p 349–360